

Numerical studies of laser cutting on an active electrode material for lithium-ion batteries

Dongkyoung Lee, and Jyotirmoy Mzaumder

Citation: **ICALEO 2011**, 60 (2011); doi: 10.2351/1.5062300

View online: <https://doi.org/10.2351/1.5062300>

View Table of Contents: <https://lia.scitation.org/toc/ica/2011/1>

Published by the [Laser Institute of America](#)

ARTICLES YOU MAY BE INTERESTED IN

[Parameter optimization for high speed remote laser cutting of electrodes for lithium-ion batteries](#)

Journal of Laser Applications **28**, 022006 (2016); <https://doi.org/10.2351/1.4942044>

[Three dimensional simulation of high speed remote laser cutting of cathode for lithium-ion batteries](#)

Journal of Laser Applications **28**, 032010 (2016); <https://doi.org/10.2351/1.4950908>

[Numerical studies of laser cutting of an anode for lithium-ion batteries](#)

International Congress on Applications of Lasers & Electro-Optics **2012**, 1252 (2012); <https://doi.org/10.2351/1.5062418>

[Investigation of different laser cutting strategies for sizing of Li-ion battery electrodes](#)

International Congress on Applications of Lasers & Electro-Optics **2012**, 908 (2012); <https://doi.org/10.2351/1.5062562>

[The numerical studies of the laser processing parameters on copper and aluminum during laser cutting](#)

International Congress on Applications of Lasers & Electro-Optics **2010**, 239 (2010); <https://doi.org/10.2351/1.5062032>

NUMERICAL STUDIES OF LASER CUTTING ON AN ACTIVE ELECTRODE MATERIAL FOR LITHIUM-ION BATTERIES

P#107

Dongkyoung Lee^{1,2}, Jyotirmoy Mzaumder^{1,2,3}

¹NSF Center for Lasers and Plasmas in Advanced Manufacturing

²Department of Mechanical Engineering, ³Department of Materials Science and Engineering
University of Michigan at Ann Arbor, MI, 48109-21215, USA

Abstract

One of the challenges during the lithium-ion battery manufacturing process is the sizing of electrodes with good cut surface quality. If the sizing process provides poor cut surface quality, internal short circuits in the cells and significant heat generation, which affect battery performance, occur. Currently, electrodes are sized using mechanical cutting by rotary knives and dies, which could result in delamination, burrs, and edge bending. The laser cutting of electrodes could improve the cut surface quality with high speed because of its high energy concentration, small heat affected zone, fast processing time, high precision, contact free process, and flexible range of laser power. However, without understanding the underlying physics, these advantages might not be fully utilized. Electrodes are composed of current collectors and active electrode materials, such as graphite-coated copper and lithium metal oxide-coated aluminium for anodes and cathodes respectively. To analyze the laser cutting of these electrodes, understanding the laser cutting for each material is an essential step. In this study, a 3D self-consistent laser cutting model is adopted and solved numerically for graphite laser cutting. This model includes multiple physical phenomena, such as multiple reflections, heat transfer, surface tension, recoil pressure, and phase changes. The effect of laser power and scanning speed on graphite during the laser cutting is analyzed. Furthermore, the influence of the sublimation of graphite during the laser cutting is observed.

Introduction

The automotive industry focuses on clean propulsion systems to achieve high fuel efficiency and satisfy environmental regulations. To obtain these requirements, their propulsion

systems are rapidly transitioning from solely gasoline and diesel engines to battery-based hybrid engines to accommodate an expanding market. According to a report by The Boston Consulting Group [1], electric and hybrid cars may be sold in 2020 in the world's four largest automotive markets of North America, Japan, China, and Western Europe.

Battery-based engines, such as those in hybrid electric vehicles (HEVs), plug-in hybrid electric vehicles (PHEVs), and electric vehicles (EVs), are either on the market or under development. One of the factors enabling development of such vehicles is advanced battery technology. Among the battery technologies, it is believed that lithium-ion batteries are the most promising battery technology due to its advantages of a high energy density, lack of memory effects, and slow loss of charge when not in use [2]. Electrodes for lithium-ion batteries consist of active electrode material and current collector material. The active electrode material is coated on both sides of the current collector material, as shown in Figure 1 and Figure 2. The active electrode materials are typically graphite and lithium-metal oxides (e.g., LiFePO_4 , LiCoO_2 , LiMn_2O_4) for anode and cathode, respectively. The current collector materials are copper and aluminum for anode and cathode, respectively.

While the choice of chemistry is one of the most important factors affecting the performance of lithium-ion batteries, manufacturing process is also a significant factor. The manufacturing process of lithium-ion batteries is briefly introduced as follows

1. Select the appropriate active electrode and current collector materials
2. Mix a polymeric binder, solvent, and active electrode power material to create a slurry.

3. Produce positive and negative electrodes by coating a thin film of the slurry on both sides of the current collector materials, as shown in Figure 2.
4. Cut the electrodes to the desired dimensions.
5. Stack the electrodes using separators, place them in respective cases, fill them with electrolytes, and finally seal them.

Currently, die cutting and rotary knife slitting are used to stamp planar electrodes for prismatic cells and to size electrode strips for cylindrical cells, respectively. These current cutting processes require relatively expensive tooling that wears over time. Tool wear causes process instabilities and poor cut quality, which is characterized by burrs, edge bending, micron sized material attachments and delamination. These poor cut qualities can result in internal short circuits and heat concentration, which give rise to catastrophic failures of the system. Thus, the cut quality affects the performance of the lithium-ion battery significantly.

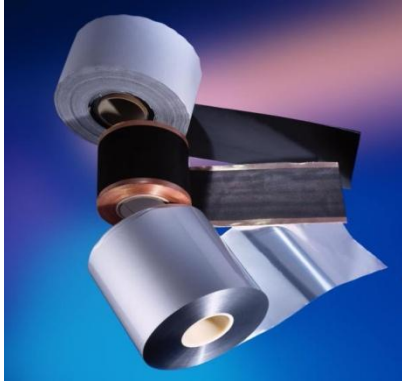


Figure 1. Electrode material for lithium-ion batteries (Fraunhofer-ISIT)

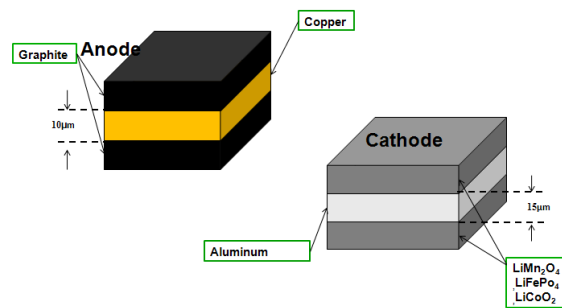


Figure 2. Configuration of electrodes.

Laser cutting can provide cut surfaces of good quality with fast process time due to its high energy concentration, contact-free process, and

flexible power range. Although laser cutting is the most common industrial application [3], the application of laser cutting to size the lithium-ion battery has been investigated by few researchers. Achievable cutting speed and cut quality of the electrodes for the lithium-ion battery were studied with a pulsed solid state laser and a single mode fiber laser in combination with fixed optics and 2D scanning optics [4]. High speed laser cuttings of electrodes for the lithium-ion battery using single mode fiber lasers were investigated. This study illustrated the achievable highest cutting speed, the effect of the focus beam and the number of cutting passes [5]. A comparison between a CW laser and a pulsed laser cutting of electrodes for lithium-ion batteries was examined. Achievable cutting speeds, qualities, and the application areas for the two operating modes were also discussed [6]. These experimental conclusions have been derived through a trial and error process. Investigating underlying physical phenomena with numerical analysis provides significant impacts to fully utilize the laser cutting of electrodes for lithium-ion batteries.

Since electrodes are a sandwiched composite material, the interface of the each material needs to be carefully treated. Prior to considering the sandwiched composite material directly, understanding the behaviors of each material is a crucial step. Numerical studies of the laser cutting of current collector materials for the lithium-ion battery were examined [7]. In the current study, numerical studies of the laser cutting of an active electrode material for the lithium-ion battery are investigated. This study only considers the active electrode material for the anode, which is graphite, since material properties of lithium-metal oxide are unavailable. Moreover, an initial penetration of the cutting process is focused due to limitations of computation domain and time. This paper is composed as follows. First, a mathematical model of laser-material interaction is introduced with assumptions. Second, results obtained with different combinations of laser parameters are discussed in terms of interaction time, penetration depth, and the geometry of the penetration hole. Finally, a conclusion will follow.

Mathematical model

A mathematical modeling of pure material can be done in the similar way to the steel substrate with little modification. The three-dimensional self-consistent laser-material interaction model on the steel substrate is developed by Ki [8]. Based on his work, modifications are accomplished to model laser cutting on graphite substrates. The mathematical modeling is described and modification will be mentioned in the following sections.

Governing equations

This study assumes an incompressible, laminar and Newtonian liquid flow. Vaporization processes are treated as the volume source. Continuity, momentum transfer, energy transfer can be expressed by following governing equations.

$$\nabla \cdot \mathbf{u} = \frac{\dot{m}_{evap}}{\rho} \delta(\phi) \quad (1)$$

$$\frac{\partial(\rho u)}{\partial t} + \nabla \cdot (\rho \mathbf{u} \mathbf{u}) = \mu \nabla^2 u - \frac{\partial p}{\partial x} - \mathbf{e}_x \cdot (\sigma \mathbf{n} \kappa - \Delta_s T \frac{d\sigma}{dT}) \delta(\phi) \quad (2)$$

$$\frac{\partial(\rho v)}{\partial t} + \nabla \cdot (\rho \mathbf{u} \mathbf{v}) = \mu \nabla^2 v - \frac{\partial p}{\partial y} - \mathbf{e}_y \cdot (\sigma \mathbf{n} \kappa - \Delta_s T \frac{d\sigma}{dT}) \delta(\phi) \quad (3)$$

$$\frac{\partial(\rho w)}{\partial t} + \nabla \cdot (\rho \mathbf{u} \mathbf{w}) = \mu \nabla^2 w - \frac{\partial p}{\partial z} - \mathbf{e}_z \cdot (\sigma \mathbf{n} \kappa - \Delta_s T \frac{d\sigma}{dT}) \delta(\phi) \quad (4)$$

$$\frac{\partial(\rho \bar{C}_{pl} T)}{\partial t} + \mathbf{u} \cdot \nabla (\rho \bar{C}_{pl} T) = \nabla \cdot (k \nabla T) - L \frac{\partial(\rho f_l)}{\partial t} + \frac{\partial(\rho f_s \Delta \bar{C}_p T)}{\partial t} + \dot{q}^*(t, \mathbf{x}) \delta(\phi) \quad (5)$$

where \mathbf{u} is the liquid velocity vector, \mathbf{x} is the spatial vector, ρ is the density, μ is the viscosity, p is the pressure, k is the thermal conductivity, \bar{C}_{pl} is the average-specific heat of liquid, t is the

time, f_l is the liquid mass fraction and $\delta(\phi)$ is the delta function to incorporate boundary conditions. Third terms on the right hand side of Eqs. (2)-(4) are boundary conditions for the L/V interface. Ki [8] derived the thermo-capillary force based on Sussman's model [9] and this model also contains both the capillary and thermo-capillary forces. The second and third terms on the right hand side of Eq. (5) are the boundary conditions for energy equations on the S/L interface. This is adopted from Bennon's continuum model [10]. The solid mass fraction is defined as

$$f_s = 1 - f_l \quad (6)$$

Similarly, the volume fraction can be defined for liquid and solid (g_l and g_s). The relationship between the mass fraction (f_l) and the volume fraction (g_s) can be described as

$$f_s = \frac{\rho_s g_s}{\rho} \quad (7)$$

$$f_l = \frac{\rho_l g_l}{\rho} \quad (8)$$

$$g_s + g_l = 1 \quad (9)$$

With these relations, the density (ρ), thermal conductivity (k), and enthalpy (h) for the liquid and solid mixture are defined as

$$\rho = g_s \rho_s + g_l \rho_l \quad (10)$$

$$k = \left(\frac{g_s}{k_s} + \frac{g_l}{k_l} \right)^{-1} \quad (11)$$

$$h = f_s h_s + f_l h_l \quad (12)$$

While Ki [8] obtained mass liquid fraction from iron based on an assumption of the binary alloy material, this study assigns the mass liquid fraction 1 and 0 when the temperature is above and below melting temperature, respectively.

This is because pure materials have been selected. The phase enthalpies are obtained as

$$h_s = \int_0^T C_{ps} dT \quad (13)$$

$$h_l = \int_0^{T_m} C_{ps} dT + L_m + \int_{T_m}^T C_{pl} dT \quad (14)$$

where T_m is the melting temperature, L_m is the latent heat of fusion, C_{pl} is the constant-pressure specific heat of liquid, C_{ps} is the constant-pressure specific heat of the solid. Furthermore, the average specific heats of solid and liquid (\bar{C}_{ps} and \bar{C}_{pl}) are defined as

$$\bar{C}_{ps} = \frac{1}{T} \int_0^T C_{ps} dT \quad (15)$$

$$\bar{C}_{pl} = \frac{1}{T - T_m} \int_{T_m}^T C_{pl} dT \quad (16)$$

$$h_s = \bar{C}_{ps} T \quad (17)$$

$$\begin{aligned} h_l &= \bar{C}_{ps} T_m + L_m + \bar{C}_{pl} (T - T_m) \\ &= \bar{C}_{pl} T + L \end{aligned} \quad (18)$$

$$\bar{C}_p = \bar{C}_{pl} - f_s (\bar{C}_{pl} - \bar{C}_{ps}) \quad (19)$$

Where $L = (\bar{C}_{ps} - \bar{C}_{pl}) T_m + L_m$. By using the defined mixture variables, the boundary conditions for S/L interface can be calculated [11]. A fourth term on the right hand side of Eq. (5), is added into the energy conservation equation as the boundary condition of the L/V interface in Eq. (5). The multiple reflections section will describe a detailed explanation of this term.

Level Set Equation for the L/V Interface Tracking

A key factor in the investigation of the interface shape and the process physics is tracking free surface. Osher and Sethian [12] developed the level set method. This method has increasingly been used for many complex problems due to its easy implementation, straightforward concept, ability to handle surface merging and separation automatically, and easy achievements of geometric qualities, such as the surface normal and the curvature on the surface.

To implement the level set method, the surface of interest, which is the L/V interface, is set as the zero iso-surface or zero level set. However, the equations are valid for both a zero level set, as well as all other level sets [13].

$$\phi(\mathbf{x}, t) = \pm d \quad (20)$$

To derive PDE, d in Eq.(20) is set to zero and the material derivative is taken as

$$\frac{D\phi}{Dt} = \frac{\partial \phi}{\partial t} + \mathbf{u} \cdot \nabla \phi = 0 \quad (21)$$

This equation can be re-written as

$$\frac{\partial \phi}{\partial t} + \mathbf{u} \cdot \mathbf{n} |\nabla \phi| = 0 \quad (22)$$

Since surface normal vectors can be obtained from the level set function as

$$\mathbf{n} = \frac{\nabla \phi}{|\nabla \phi|} \quad (23)$$

Here, $\mathbf{u} \cdot \mathbf{n}$ is the speed of the interface in the normal direction and F is referred to as the speed function or force function. Thus, the final form of the level set function is a hyperbolic PDE.

$$\frac{\partial \phi}{\partial t} + F |\nabla \phi| = 0 \quad (24)$$

The speed function, or F , is composed of numerical expression of vaporization and fluid flow. This will be discussed later in detail.

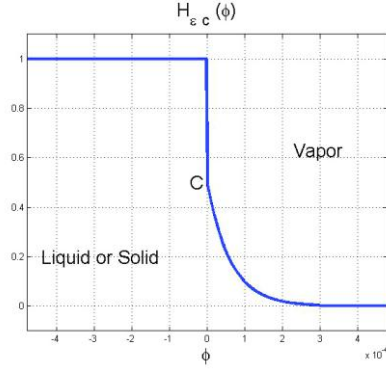


Figure 3. Material properties at L/V interface

Modeling of L/V interface phenomena

First, the L/V interface has significantly different properties to those of the S/L interface. Therefore, the material properties are smoothed out from the liquid to the vapor phase using discrete functions proposed as

$$H_{\epsilon,c}(\phi) = \begin{cases} 1 & \text{if } \phi \leq 0, \\ c \left(\frac{1}{2} \right)^{\frac{\phi}{\min(\Delta z)}} & \text{if } 0 < \phi \leq \epsilon, \\ 0 & \text{if } \phi > \epsilon, \end{cases} \quad (25)$$

where ϵ and c represent the width of the interface and the degree of continuity, respectively. The c ranges from 0 to 1. Thus, the material properties can be expressed by this function. This is shown in Figure 3. Viscosity, for example, is defined as

$$\mu_{\epsilon,c} = \mu_{vap} + (\mu_{liq} - \mu_{vap}) H_{\epsilon,c}(\phi) \quad (26)$$

Second, in the laser-material interaction processes, the L/V interface in the level set equation, i.e. $\phi = 0$, is evolved on the basis of fluid flow and vaporization. The fluid flow can be obtained by solving momentum equation proposed in Equation (3). To implement vaporization into the level set equation, jump conditions with back pressure is used to take into account discontinuity at the interface cause by the Knudsen layer [14]. The net mass flux and energy flux [14-16] can be obtained as

$$\dot{m}_{evap}'' = \rho_s \sqrt{\frac{RT_s}{2\pi}} - \rho_v \sqrt{\frac{RT_v}{2\pi}} \beta F_-(m) = \rho_l F_{evap}'' \quad (27)$$

$$\dot{q}_{evap}'' = \rho_l L_v F_{evap}'' \quad (28)$$

where

$$m = \frac{u_v}{\sqrt{2R_v T_v}}$$

$$F_- = \sqrt{\pi m} [-1 + \text{erf}(m)] + \exp(-m^2)$$

$$G_- = (2m^2 + 1)[1 - \text{erf}(m)] - \frac{2}{\sqrt{\pi}} m \exp(-m^2)$$

$$\beta = \frac{2(2m^2 + 1)\sqrt{T_v/T_s} - 2\sqrt{\pi m}}{F_- + \sqrt{T_v/T_s} G_-}$$

Hence, a final form of the speed function is

$$F = F_{evap} + \mathbf{u} \cdot \mathbf{n} \quad (29)$$

where \mathbf{u} is the melt pool speed and \mathbf{n} is the normal vector. The vaporizing mass flux, F_{evap} , is assumed perpendicular to the L/V interface.

Absorption coefficient and multiple reflections with incident angle

The energy absorbed on a flat material surface varies depending on the materials, temperature and wavelength. However, when the deep penetration hole exists, total energy transfer from the laser beam to a workpiece is increased significantly due to the multiple reflections inside the walls of the hole. These multiple reflections can be realized by using the ray tracing method. If the laser beam is irradiated on the wall of the deep penetration hole, then the reflected rays can be calculated by the formula

$$\mathbf{r} = \mathbf{i} + 2(-\mathbf{i} \cdot \mathbf{n})\mathbf{n} \quad (30)$$

where, \mathbf{r} is the reflected ray, \mathbf{i} is the incoming ray, and \mathbf{n} is the surface unit normal. As mentioned earlier, the level-set method provides a surface unit normal vector at each point.

Table 1. Material properties of Graphite

Property	value
Sublimation temperature (T_b)	4800(K)[17]
Critical point temperature (T_{cr})	7811(K) [18]
Solid density (ρ_s)	1730(Kg/m ³)[19]
Latent heat of sublimation (L_v)	5.98E+07(J/kg) [19]
Solid thermal conductivity (k_s)	18.1(W/mK) [19]
Solid constant-pressure specific heat (C_{ps})	2092.48(J/kgK) [19]
Solid thermal diffusivity (α_s)	5.00E-06(m ² /s) [19]
Laser absorptivity for flat surface (A_0)	0.81

In this method, the laser energy is absorbed into the wall at each reflection. When the rays escape the computational domain, the calculation of the multiple reflections is terminated. In addition, incident angle is taken into account in determining the absorption coefficient, as suggested by Fabbro and Chouf [20]. It is presented as following

$$A(\alpha) = A_0(\cos \alpha)^q \quad (31)$$

Where, α is the incident angle, A_0 is the absorption coefficient on flat surface, and q is the characteristic of the material. Again, the incident angle can be calculated based on the information from the level-set method. The values of the material characteristics, such as for A_0 and q , vary based on the material properties. The multiple reflections contribute a large portion of the laser energy absorption in the deep penetration hole during laser material interaction and it increases absorption dramatically compared to the absorption on the flat surface. This increased energy absorption by multiple reflections causes the metal to behave as a black body. Effects of this absorption mechanism are clearly seen in this paper.

After considering energy absorption by multiple reflections, energy losses due to evaporation and radiation on the L/V interface, the actual net energy influx at the interface is

$$\dot{q}'' = \dot{q}_{L/V}'' - \dot{q}_{evap}'' - \sigma \varepsilon (T^4 - T_\infty^4) \quad (32)$$

Where $\dot{q}_{L/V}''$ is the spatial laser beam distribution after multiple reflections $\sigma \varepsilon (T^4 - T_\infty^4)$ is energy loss due to radiation, σ and ε are Stefan-Boltzmann constant and emissivity, respectively. Note that the simultaneous calculation of the vapor phase and the liquid phase allows for the exclusion of convection heat loss [8].

Modification for sublimation

With assumption that there is no liquid phase on the graphite laser cutting, abovementioned theoretical model become simpler. To keep demonstrate the important physical phenomena included in the three-dimensional self-consistent laser-material interaction model, modification is carefully made.

First, since there is no liquid phase, no mushy zone is considered. Second, a liquid viscosity is assumed to be a large number compared to the gas phase because Eqs. (2)-(4) are modelled to solve the both liquid and gas phases. Third, liquid properties are set to be the same as solid properties. Finally, no surface tension is considered.

Results and discussions

Simulation preparation and solutions schemes

The simulation domain is 75 μ m x 30 μ m x 90 μ m. Non-uniform mesh size is used and the smallest discrete mesh size is 0.42857 μ m. The governing equations are discretized using an implicit finite difference method [21]. The Semi-Implicit Method for Pressure-Linked Equation Consistent

(SIMPLEC) with a staggered grid is adapted to obtain a proper pressure field [22]. The Conjugated Gradient Stabilized (CGSTAB) method is used to solve the matrix equations. Moreover, a second-order space convex scheme is utilized to discretize the spatial derivative of the level set equation. A CW single mode YAG laser with a Gaussian beam and the diameter of 11 μ m is assumed and moves in the x-direction. To smooth the materials properties on the L/V interface, the values of c and ϵ for all of the material properties were taken as 1 and 7 X min(Δz), respectively. Graphite is chosen as a substrate material and its properties are listed in Table 1. The thickness of the graphite is 35 μ m. The range of the laser parameters are 50W to 450W for the laser power and 1000 mm/s to 5000 mm/s for the scanning speed. The combination of the laser parameters are tabulated in Table 2. The penetration time is obtained when the depth of a deep penetration hole reaches the thickness of the substrate. This case is called a full penetration.

Table 2. Laser parameters

Sim #	Laser parameters	
	Power(w)	Speed(mm/s)
1	200.00	5000
2	250.00	
3	300.00	
4	350.00	
5	400.00	
6	450.00	3000
7	100.00	
8	150.00	
9	200.00	
10	250.00	
11	300.00	1000
12	50.00	
13	100.00	
14	150.00	
15	200.00	
16	250.00	

Effects of the laser parameters on penetration time

The simulation results are shown in Table 3. Although both partial and full penetration were observed during the laser cutting of copper and aluminium within the given range of the laser parameters [23], full penetration is obtained for every case during the laser cutting of the graphite. Since the absorption coefficient of graphite is 0.81, which is 16.2 and 11.6 times greater than that of aluminium and copper, the given range of the laser parameters provides enough laser power density to have full penetration.

The penetration times for full penetration are between 0.0337 and 0.2575 μ s, which are very fast interactions compared to the copper and aluminum cases [23]. Since this study obtained full penetration for all cases, the effects of the laser parameters to the penetration time can be investigated. Figure 4 shows the penetration times depending on laser power density with its fit line. First of all, the penetration time decreases exponentially as increasing the laser power density. This relationship is expressed as $t_p = 10^{10} I^{-0.916}$, where I is the power density and t_p is the penetration time. Based on this function, the penetration time can be predicted. Second, there is almost no effect of scanning speed on penetration time. This fact is more clearly seen in Figure 5, where the penetration times dependent on the scanning speed with different laser powers are shown. It is clear that each laser power provides a specific corresponding penetration time at a specific fixed scanning speed. For example, with the chosen scanning speed of 3000 mm/s, 5 different penetration times are obtained with 5 different laser powers, which vary from 100W to 300W with the increment of 50W. However, no difference is observed in the case of the variation of the scanning speed with the fixed laser power. With the selected laser power of 200W, the penetration times of 1000 and 5000 mm/s are the same. The penetration time of 3000 mm/s is 0.0699 μ s, which is only a difference of 0.43% compared to that of the 1000 and 5000 mm/s scanning speeds. With the selected laser power of 250W, it also shows a very similar relationship to the case of the laser power of 200W. Therefore, the laser cutting of the graphite within the given range of the laser

power is a highly laser-power-density-dependent process.

Table 3. Penetration time

sim #	Penetration time (μs)
1	0.0702
2	0.0573
3	0.0487
4	0.0424
5	0.0375
6	0.0337
7	0.1307
8	0.0908
9	0.0699
10	0.0573
11	0.0487
12	0.2575
13	0.1311
14	0.0914
15	0.0702
16	0.0576

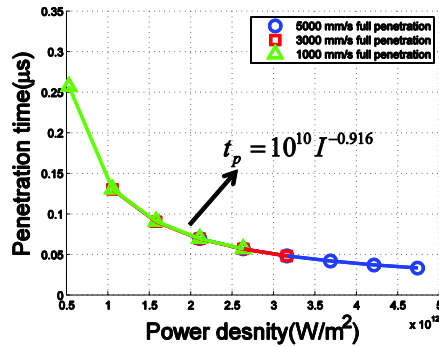


Figure 4. Penetration time VS power density

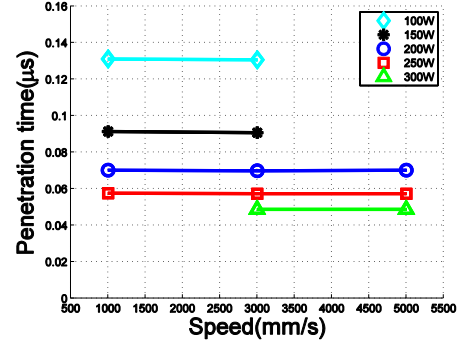


Figure 5. Penetration time VS scanning speed

Characteristics of the laser cutting of graphite

To investigate the characteristics of the laser cutting of graphite, we focus on the 3000 mm/s scanning speed cases since all the simulation results show very similar behaviors. The penetration of the hole during laser cutting is shown in Figure 6. The early stage of the laser cutting shows an exponential increase of penetration depth. After this increase, the penetration depth increases almost linearly. Figure 7 shows the variation of the absorptivity. Its value increases very sharply and then increases gradually when the value is over 0.95. The average number of reflections is shown in Figure 8. Its value increases linearly until it reaches the maximum number of reflections, which is between 3 and 3.5. These three figures are closely related.

The multiple reflections can explain the behavior of the penetration depth by observing the variation of the absorptivity. At the early stage of laser cutting, laser energy is absorbed on the flat surface without multiple reflections. Thus, absorptivity is almost similar to the absorption coefficient of the flat surface, which is 0.81. Once a deep penetration hole exists, the absorptivity increases very sharply, as shown in Figure 7. The increase of the absorptivity, in turn, accelerates the penetration of the hole until the depth of the deep penetration hole reaches 10μm. After the acceleration of the hole penetration, penetration depth shows a linear increase since the value of the absorptivity is always maintained at 0.95. Although a high value of absorptivity is obtained, the number of reflections is low, as can be seen from the Figure 8. This phenomenon can be explained by the

value of absorptivity. Low laser energy is reflected on the interface due to the high value of the absorption coefficient of graphite. Thus, graphite can absorb the 98% of the laser energy even with a relatively small number of reflections.

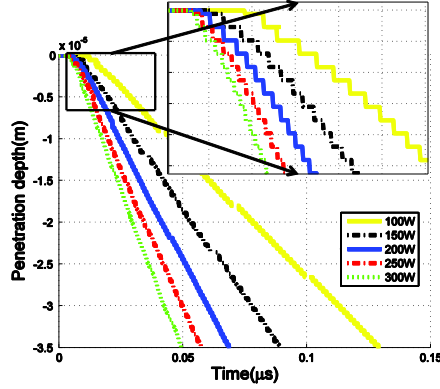


Figure 6. Penetration depth for the scanning speed of 3000 mm/s

Figure 9 and Figure 10 respectively present the temperature and intensity distributions of the laser cutting of the graphite with a scanning speed of 3000 mm/s and laser power of 200W. The interface of the deep penetration hole is very smooth and clear during the entire simulation since no liquid exists. This indicates that sublimation plays a key role to form the smooth interface geometry. High temperature is observed on the both front and rear wall as shown in Figure 9, because of multiple reflections. The intensity distribution in Figure 10 shows that multiple reflections are achieved near the tip of the deep penetration hole. This explains again why the average number of reflections is relatively low due to the high value of the absorption coefficient.

Conclusion

To investigate the cut quality of the surface during the laser cutting of electrodes for lithium-ion batteries, a 3D self-consistent mathematical model of the laser cutting of an active electrode material is developed as an initial step with modifications of Ki's model [21]. Modification is done as follows, First, no mushy zone is

considered. Second, a liquid viscosity is assumed to be a large number compared to the gas phase. Third, liquid properties are set to be the same as solid properties. Finally, no surface tension is considered. Thus, this modified model includes multiple physical phenomena, such as multiple reflections, heat transfer, recoil pressure, and phase changes.

The effects of the laser parameters to the penetration time can be investigated. The penetration time decreases exponentially as the laser power density increases. However, there is almost no effect of scanning speed on penetration time. Therefore, the laser cutting of the graphite within the given range of the laser parameters is a highly laser-power-density-dependent process.

The 3000 mm/s scanning speed cases are chosen to investigate the characteristics of the laser cutting of graphite. Once the penetration hole exists at the early stage of the laser cutting, absorptivity increases sharply due to the multiple reflections. Thus, the early stage of the laser cutting shows an exponential increase of penetration depth. When the absorptivity is over 0.95, most of the laser energy is absorbed by a small number of reflections, which is also clearly seen in the 3D intensity distribution. Therefore, the absorptivity increases gradually and the penetration depth increases linearly. Finally, the 3D temperature and intensity distributions show that sublimation plays a significant role in the formation of the smooth and clean interface.

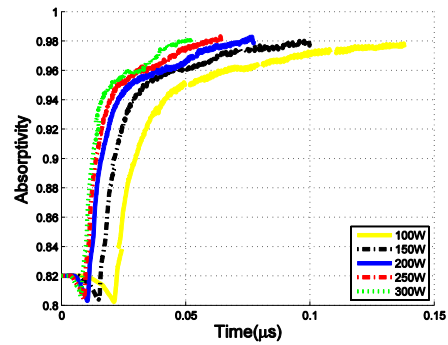


Figure 7. Absorptivity for the scanning speed of 3000 mm/s

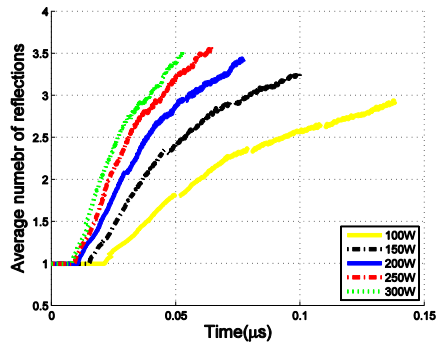


Figure 8. Average number of reflections for the scanning speed of 3000 mm/s

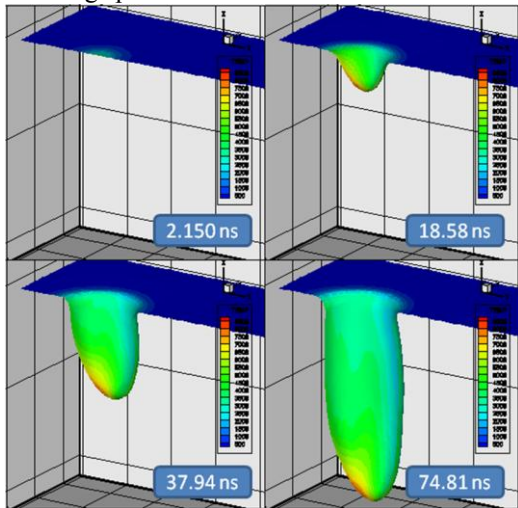


Figure 9. 3D temperature distribution of the graphite for the scanning speed of 3000 mm/s and the laser power of 200W

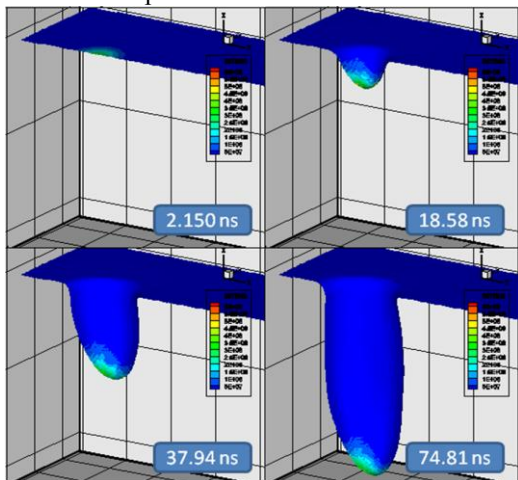


Figure 10. 3D intensity distribution of the graphite for the scanning speed of 3000 mm/s and the laser power of 200W

Acknowledgement

This work was made possible by financial support from a joint program on Alternative Energy Technology for Transportation between Fraunhofer Institute of Germany and University of Michigan. Laser cutting work for model validation was carried at Fraunhofer Center for Laser Technology at Plymouth, Michigan. Electrode testing was carried out by Fh.G ICT in Karlsruhe in Germany.

References

- [1] The comeback of the electric car? How real, how soon, and what must happen next. Boston consulting group report; (2009).
- [2] Alamgir M, Sastry AM. Efficient Batteries for Transportation Applications. SAE Convergence. Detroit, MI (2008).
- [3] Steen WM, Mazumder J, SpringerLink (Online service). Laser Material Processing. 4th Edition. ed. London: Springer-Verlag London; (2010).
- [4] Herfurth HJ, Patwa R, Pansar H. Laser Cutting of Electrodes for Advanced Batteries. Proceedings of the LPM. Germany(2010).
- [5] Patwa R, Herfurth HJ, Pansar H, Heinemann S, Mazumder J, Lee D. High speed laser cutting of electrodes for advanced batteries. Proceedings of the ICALEO. Anaheim, CA(2010).
- [6] Luetke M, Franke V, Techel A, Himmer T, Klotzbach U, Wetzig A, et al. A Comparative Study on Cutting Electrodes for Batteries with Lasers. Physics Procedia.(2011);12:286-91.
- [7] Lee D, Mazumder J. The Numerical Studies of the Laser Processing Parameters on Copper and Aluminum during Laser Cutting. Icaleo 2010. Anaheim, California: Laser institute of America; (2010).
- [8] Ki H, Mohanty PS, Mazumder J. A numerical method for multiphase incompressible thermal flows with solid-liquid and liquid-vapor phase transformations. Numerical Heat Transfer Part B-Fundamentals. (2005);48:125-45.
- [9] Sussman M, Smereka P, Osher S. A level set approach for computing solutions to incompressible two-phase flow. J Comput Phys. (1994);114:146-59.

- [10] Bennon WD, Incropera FP. A continuum model for momentum, heat and species transport in binary solid-liquid phase change systems--I. Model formulation. *International Journal of Heat and Mass Transfer*. (1987);30:2161-70.
- [11] Ki H, Mohanty PS, Mazumder J. Modeling of laser keyhole welding: Part I. Mathematical modeling, numerical methodology, role of recoil pressure, multiple reflections, and free surface evolution. *Metallurgical and Materials Transactions a-Physical Metallurgy and Materials Science*. (2002);33:1817-30.
- [12] Osher S, Sethian JA. Fronts propagating with curvature-dependent speed: Algorithms based on Hamilton-Jacobi formulations. *Journal of Computational Physics*. (1988);79:12-49.
- [13] Sethian JA. Level set methods and fast marching methods. 2nd ed. Cambridge: Cambridge University Press; (1999).
- [14] Knight CJ. THEORETICAL MODELING OF RAPID SURFACE VAPORIZATION WITH BACK PRESSURE. *Aiaa Journal*. (1979);17:519-23.
- [15] Ki H, Mohanty PS, Mazumder J. Modelling of high-density laser-material interaction using fast level set method. *Journal of Physics D-Applied Physics*. (2001);34:364-72.
- [16] Ytrehus T, Ostmo S. Kinetic theory approach to interphase processes. *International Journal of Multiphase Flow*. (1996);22:133-55.
- [17] Musella M, Ronchi C, Brykin M, Sheindlin M. The molten state of graphite: An experimental study. *Journal of Applied Physics*. (1998);84:2530-7.
- [18] Leider HR, Krikorian OH, Young DA. Thermodynamic properties of carbon up to the critical point. *Carbon*. (1973);11:555-63.
- [19] Shusser M. Kinetic theory analysis of laser ablation of carbon: Applicability of one-dimensional models. *Journal of Applied Physics*. (2007);101.
- [20] Fabbro R, Chouf K. Keyhole modeling during laser welding. *Journal of Applied Physics*. (2000);87:4075-83.
- [21] Ki H. Modeling and measurement of processes with liquid-vapor interface created by high power density lasers(2001).
- [22] Patankar SV. Numerical heat transfer and fluid flow. Washington, New York: Hemisphere Pub. Corp. ;McGraw-Hill; (1980).
- [23] Lee D, Mazumder J. The Numerical Studies of the Laser Processing Parameters on Copper and Aluminum during Laser Cutting. *Proceedings of the ICALEO*. Anaheim, California: Laser institute of America; (2010).

Meet the Author(s)

Dongkyoung Lee graduated in 2006 with a B.S. in Mechanical Engineering from Hanyang University in Seoul, Korea. He then earned his M.S. through research working on the dynamics and control of aerial rotorcraft in Aerospace Engineering at the University of Michigan – Ann Arbor in 2007. He is currently a Ph. D student in Mechanical Engineering at the University of Michigan – Ann Arbor. His main research interest is understanding of various physical phenomena during laser-material interaction such as phase changes of materials, liquid metal movements, effect of material properties, and plasma absorption, into computational simulation. With these simulation results, he is developing correlations between these physical phenomena during the laser-material interaction and experimentally obtained final products to improve quality of manufacturing processes.

Jyoti Mazumder is Robert H. Lurie Professor of Engineering in the Department of Mechanical Engineering and Materials Science and Director of the Center for Laser Aided Intelligent Manufacturing at the University of Michigan in Ann Arbor. He has published more than 325 papers and edited/co-edited 9 books on topic related to laser materials processing. He is also taking his research to market by commercializing DMD through a start up called POM Group Inc, where he acts as CEO. Dr. Mazumder has received numerous awards and honors for his research including, Schawlow Award for seminal contribution to Laser application research from Laser Institute of America in 2003 and William Ennor Award for manufacturing from ASME in 2006. Adams memorial membership Award from AWS, 2007 and Thomas Edison Award from ASME in 2010. He served as the president of the Laser Institute of America in the year 2000. Dr. Mazumder was Editor in Chief of the *Journal of Laser Application* until December 2009.